Open Archive Toulouse Archive Ouverte (OATAO)

OATAO is an open access repository that collects the work of Toulouse researchers and makes it freely available over the web where possible.

Any correspondence concerning this service should be sent to the repository administrator: staff-oatao@inp-toulouse.fr

Molecular Clusters in Mesoporous Materials as Precursors to Nanoparticles of a New Lacunar Ternary Compound Pd_xMo_yP

S. Grosshans-Vièles · P. Croizat · J.-L. Paillaud ·
P. Braunstein · O. Ersen · J. Rosé · B. Lebeau ·
P. Rabu · C. Estournès

Abstract Bimetallic clusters of composition $Pd_2Mo_2(\eta^5\text{-}C_5H_5)_2(\mu_3\text{-}CO)_2(\mu_2\text{-}CO)_4$ $(PR_3)_2$ (R = ethyl or phenyl) were incorporated by impregnation from solution into two different silica matrices, amorphous xerogels and ordered SBA-15, and a study of their thermal decomposition under a reducing atmosphere is reported. With both matrices, a suitable thermal treatment afforded nanoparticles of a new bimetallic phosphide. Although nanoparticles of composition Pd_xMo_yP, isostructural with Mo_3P, were formed in both matrices, they were more uniformly distributed in the

S. Grosshans-Vièles · J.-L.Paillaud (✉) · B. Lebeau
Laboratoire de Matériaux à Porosité Contrôlée (UMR 7016 CNRS, ENSCMu, UHA),
3 rue Alfred Werner, 68093 Mulhouse Cedex, France
e-mail: Jean-Louis.Paillaud@uha.fr

S. Grosshans-Vièles · P. Croizat · P. Braunstein (✉) · J. Rosé
Laboratoire de Chimie de Coordination, Institut de Chimie (UMR 7177 CNRS),
Université Louis-Pasteur, 4 rue Blaise Pascal, 67070 Strasbourg Cedex, France
e-mail: braunst@chimie.u-strasbg.fr

O. Ersen
IPCMS-GSI, UMR 7504 (CNRS, ULP) 23, rue du Loess, BP 43, 67034 Strasbourg, Cedex 2, France

S. Grosshans-Vièles · P. Rabu (✉)
IPCMS-GMI, UMR 7504 (CNRS, ULP) 23, rue du Loess, BP 43, 67034 Strasbourg, Cedex 2,
France
e-mail: Pierre.Rabu@ipcms.u-strasbg.fr

C. Estournès (✉)
CIRIMAT UMR 5085 (CNRS, UPS, INPT), 118 route de Narbonne, 31062 Toulouse, Cedex 9,
France
e-mail: estournes@chimie.ups-tlse.fr

SBA-15 framework and showed a narrower size distribution. The samples have been characterized by powder XRD, chemical analysis, FT-IR spectroscopy, TEM and electron tomography (3D TEM).

Keywords Bimetallic clusters · Impregnation · Mesoporous silica · Nanoparticles · Metal phosphides

Introduction

Since the discovery of M41S-materials in the early 1990s [1], ordered mesoporous materials have become a new class of periodic porous solids. Mesoporous silica structures have been regarded as ideal supports owing to their high surface area, tunable pore size and organisation [2]. The SBA-15 framework synthesized by Zhao et al. [3] has a highly ordered hexagonal mesostructure with parallel channels like in MCM-41 and adjustable pores with a size in the range 5–30 nm [4]. This size regime is relevant to catalysis, since catalytically active metal particles are typically in the 1–10 nm size range and the pore sizes are then wide enough to allow facile diffusion of reactants and products.

Following the first use of heterometallic molecular clusters as precursors to catalytic nanoparticles [5], many bimetallic cluster-derived heterogeneous catalysts have been studied and shown to possess improved properties compared to monometallic nanoparticles [6, 7]. Such nanoparticles are often supported at the surface of oxides such as alumina [6, 8, 9, 10] or alumino-silicates [11]. The use of organized porous materials is more recent. Thus, catalytically active metallic nanoparticles incorporated into microporous zeolite Y have been reported [6, 12, 13] and the impregnation of mesoporous xerogel or MCM-41 with an organic solution of the bimetallic cluster $[NEt_4][Co_3Ru(CO)_{12}]$, followed by thermal treatment under an inert atmosphere, has led to highly dispersed magnetic nanoparticles under milder conditions than when conventional metal salts are used as precursors [14, 15]. Similarly, high-quality Co_2P nanoparticles have been obtained from diphosphine-substituted tetracobalt carbonyl clusters anchored into a SBA-15 matrix [16]. Transition metal phosphide nanoparticles have promising magnetic or catalytic properties [17].

The aim of this work was to investigate the possibility of generating bimetallic monodisperse nanoparticles from a well-defined Pd-Mo bimetallic cluster impregnated into a SBA-15 matrix after calcination under controlled atmosphere. Until now, the synthesis of bimetallic Pd–Mo particles has been performed in two steps consisting in successive additions of the Pd and Mo sources, respectively [8–13, 18]. The majority of them are used as catalysts for hydrodesulphurization (HDS) reactions [9–11,13], combustion of methane [12] or decomposition of NO [8]. The tetranuclear, bimetallic cluster $Pd_2Mo_2(\eta^5\text{-}C_5H_5)_2(\mu_3\text{-}CO)_2(\mu_2\text{-}CO)_4(PPh_3)_2$ appeared particularly attractive owing to its easy availability [19a, b] and its documented use as precursor to heterogeneous catalysts [5]. It was first used to form catalytic nanoparticles for the carbonylation reaction of nitroaromatics to give organic isocyanates and was found to have better performances than conventional catalysts containing these metals in the same proportions [5]. Then, the Ford Motor

Company in the US studied Mo–Pd and Mo–Pt bimetallic catalysts for abatement of automobile emissions prepared in this way: Kawi et al. adsorbed $Pd_2Mo_2(\eta^5$-$C_5H_5)_2(\mu_3$-$CO)_2(\mu_2$-$CO)_4(PPh_3)_2$ on a MgO powder [20], and after two successive heat treatments under hydrogen at 400 °C then 500 °C, a bilayered compound was produced at the surface of the MgO support which consisted of molybdenum cations interacting with the support and providing a platform for highly dispersed palladium. It is also interesting to note that the closely related cluster $[Pt_2Mo_2(\eta^5$-$C_5H_5)_2(\mu_3$-$CO)_2(\mu_2$-$CO)_4(PPh_3)_2]$ [19c] has been used as a precursor to zirconium doped mesoporous silica supported bimetallic catalysts for the hydrogenation of tetralin [21].

We report here the preparation in mesoporous silica matrices of Pd–Mo phosphide nanoparticles. The bimetallic clusters $[Pd_2Mo_2(\eta^5$-$C_5H_5)_2(\mu_3$-$CO)_2(\mu_2$-$CO)_4(PR_3)_2]$ (R = Et, Ph) [19a, b] were incorporated by impregnation into two types of silica matrices having a different distribution of mesopores: amorphous xerogels and ordered SBA-15. The samples have been characterized by powder XRD, chemical analysis, FT-IR spectroscopy, TEM and electron tomography (3D TEM). The influence of the nature of the phosphine ligands is discussed.

Experimental Section

Synthesis

Synthesis of Ordered Mesoporous Silica SBA-15

SBA-15 was synthesized according to the method of Zhao et al. [3]. The triblock copolymer poly(ethylene oxide)-poly(propylene oxide)-poly(ethylene oxide) (EO_{30}-$PO_{70}EO_{30}$) (Aldrich) (3.50 g) was dissolved in 111.75 g of water and 16.5 mL of HCl (12 M) at a temperature of 40 °C which was maintained with the aid of a thermostated bath. Then 7.425 g of $Si(OEt)_4$ (TEOS) were added with stirring. The mixture was then poured into a polypropylene bottle and warmed at 40 °C for 24 h and then at 90 °C for 24 h. The solid was filtered (not washed) and dried at 60 °C under air. At this stage, the molar composition is 1.0 SiO_2:0.017 P123:5.6 HCl:175 H_2O. Finally, the materials were calcined in a furnace at 500 °C for 4 h under air to remove the organics.

Xerogel

The impregnation of the clusters was performed on a commercial Silica gel 60 (0.063–0.200 mm, Merck).

Synthesis of the clusters $[Pd_2Mo_2(\eta^5$-$C_5H_5)_2(\mu_3$-$CO)_2(\mu_2$-$CO)_4(PEt_3)_2]$ (a) and $[Pd_2Mo_2(\eta^5$-$C_5H_5)_2(\mu_3$-$CO)_2(\mu_2$-$CO)_4(PPh_3)_2]$ (b)

The procedure were similar to those described earlier [19]. Since the reagents are air-sensitive, all the reactions were performed under nitrogen, in dried and purified solvents, using standard Schlenk techniques.

Incorporation of the Cluster

The matrices were first dried under vacuum, then poured and stirred in 10 mL of a saturated solution of **a** or **b** in CH_2Cl_2 for 24 h at room temperature. The resulting powder was filtered, washed several times with CH_2Cl_2 and dried at room temperature. Samples are referred to as **1a**, **1b** and **2a**, **2b** when a SBA-15 silica matrix (**1a** for cluster **a** and **1b** for cluster **b**) or the xerogel silica matrix (**2a** for cluster **a** and **2b** for cluster **b**) were used as hosts, respectively. After washing to remove the non-adsorbed cluster, the amount of incorporated cluster in the impregnated matrices were: sample **1a**, 0.20 g of cluster **a** in 0.98 g of SBA-15; sample **1b**, 0.20 g of cluster **b** in 1.04 g of SBA-15; sample **2a**, 0.30 g of cluster **a** in 1.20 g of xerogel; sample **2b**, 0.32 g of cluster **b** in 1.60 g of xerogel.

Although the metal atoms in the precursor cluster are already in a low oxidation state and despite the fact that the degradation of the cluster results in the loss of reductive CO, additional reducing atmosphere was considered necessary for the thermal treatments. They were performed under hydrogen, at 900 °C for 1 h.

Characterizations

Powder X-ray Diffraction Data collection (PXRD)

PXRD measurements were carried out on a filled capillary ($\varnothing = 0.3$ mm) using a STOE Stadi-P diffractometer in Debye–Scherrer geometry and equipped with a linear position-sensitive detector (6° in 2θ) and Ge monochromated $CuK_{\alpha1}$ radiation ($\lambda = 1.5406$ Å). The Cu tube was under a tension of 40 kV and an intensity of 30 mA. Indexation and unit cell parameters refinement have been performed with the STOE WinXPOW software [22].

Transmission Electron Microscopy (TEM) and Tomography (3D TEM)

Classical TEM investigations were made using a Topcon 002B-UHR electron microscope operating at 200 kV with a point-to-point resolution of 0.18 nm. The samples were previously sonicated in ethanol and deposited on a holey carbon membrane copper grid. The tilt series for 3D analysis were acquired in bright-field mode on a F20 TECNAI microscope (FEI Company) using an accelerated voltage of 200 kV and a high-tilt sample holder. Several series of 2D-TEM images were thus acquired using a 2048×2048 pixels cooled CCD array detector in different places of the grid containing typical ordered mesoporous silica. Each series of projections was collected over a tilt range between −65 and 65°, with an image recorded every 2° between −40° and 40° and 1° elsewhere, giving a total of 91 images. No apparent irradiation damage on the specimens was observed at the end of the acquisition process. During the

acquisition, the TEM parameters such as defocus, horizontal specimen shift, and specimen tilt were controlled automatically using the FEI eXplore 3D acquisition software. Before acquisition of a tilt series of typical 2D-TEM images, a drop of a solution containing well-dispersed gold nanoparticles with a calibrated diameter of 10 nm was deposited onto the holey carbon grid supporting the sample to make the data treatment easier. The data were treated for imaging processing and reconstruction by using IMOD software program from the University of Colorado [23]. Further details on the method are given in reference [24].

Chemical Analysis

In order to determine the correct phase compositions and possible inhomogeneities, two distinct techniques were applied. First, to determine the bulk chemical composition of the samples, wavelength-dispersive X-ray fluorescence spectrometer (MagiX FAST, PANalytical), microprobe analysis with a Philips XL30 FEG scanning electron microscope (SEM) equipped with a microprobe Si(Li) Oxford Inca Energy analyser and a JEOL JSM840 SEM apparatus with a microprobe Kevex Delta analyser were used. Unfortunately, both techniques gave unrealistic and non reproducible chemical analysis owing to the low loading of the element (Pd, Mo and P) in the resulting impregnated materials. The measured nanoprobe analysis was carried out by energy-dispersive spectroscopy of X-rays (EDSX) with the above Topcon 002B electron microscope equipped with a lithium drifted silicon detector.

Porosity Measurements

The N_2 sorption isotherms of the materials were measured at 77 K using a Micromeritics ASAP2010 sorption analyzer. Specific surface areas were determined according to the Brunauer–Emmett–Teller (BET) method [25]. The pore size distributions were calculated using the Barrett–Joyner–Halenda (BJH) model [26] applied on the adsorption branch of the isotherm. All the samples were previously degassed in situ at 423 K under vacuum before analysis.
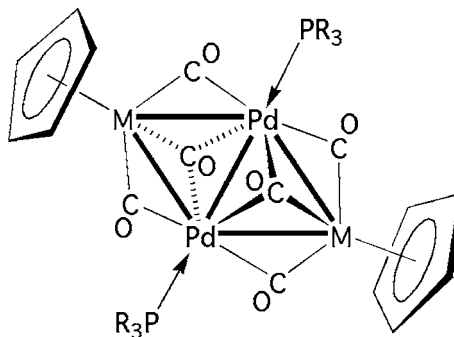
Thermogravimetric Analyses (TGA)

TGA were conducted from 25 °C to 900 °C under argon at a heating rate of 5 °C · min^{-1} with a Setaram TG-DTA 92 thermobalance.

Infrared Spectroscopy

FT-IR spectra were collected with a Digilab FTS 3000 computer driven instrument (0.5 mm thick pellet of the samples (1–2 wt.%) in KBr).

Fig. 1 Structure of the clusters $[Pd_2Mo_2(\eta^5\text{-}C_5H_5)_2(\mu_3\text{-}CO)_2(\mu_2\text{-}CO)_4(PR_3)_2]$ (R = Et, Ph)

Results and Discussion

Decomposition of the Bimetallic Clusters Under Controlled Atmosphere

The structure of the known organometallic clusters $[Pd_2Mo_2(\eta^5\text{-}C_5H_5)_2(\mu_3\text{-}CO)_2$ $(\mu_2\text{-}CO)_4(PR_3)_2]$ (R = Et, Ph) is sketched in Fig. 1 [19a]. These molecules possess a center of symmetry located at the middle of the Pd–Pd bond and the four metallic centers therefore form a planar rhombus. Each cyclopentadienyl ring is η^5-bonded to a Mo atom and to three carbon monoxide ligands, which occupy bridging positions while the Pd atoms are also connected to a phosphine ligand (PR$_3$).

The TG and DTA signals of bulk $[Pd_2Mo_2(\eta^5\text{-}C_5H_5)_2(\mu_3\text{-}CO)_2(\mu_2\text{-}CO)_4(PR_3)_2]$ are shown in Fig. 2. In both cases, R = Et and R = Ph, the carbonyl groups leave first before 170 °C and their departure is accompanied by an unexpected exotherm due to an accidental partial oxydation of the metals known to be very reactive, despite the fact that the reaction was carried out under argon. Then two steps of weight losses follow which correspond to the elimination of the ethyl or phenyl
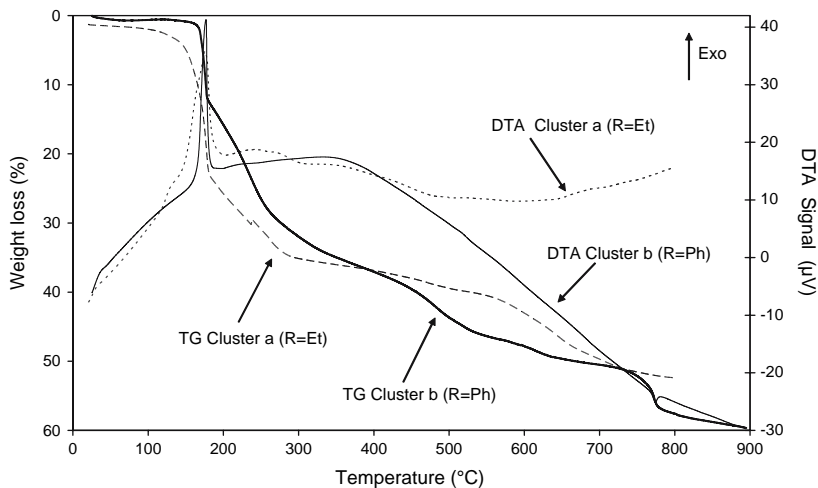

Fig. 2 TG and DTA analysis of the clusters $[Pd_2Mo_2(\eta^5\text{-}C_5H_5)_2(\mu_3\text{-}CO)_2(\mu_2\text{-}CO)_4(PR_3)_2]$ with R = Et or Ph

groups of the phosphine ligands and of the cyclopentadienyl moieties. With the triethylphosphine cluster **a**, the total weight loss up to 800 °C is about 53%. This exceeds the corresponding calculated total organic mass percentage i.e. 50.3 (6 CO, 2 Cp and 6 R with R = Et), which may be explained by the sublimation of phosphorous-containing phases at elevated temperatures. For the corresponding triphenylphosphine cluster **b**, the TGA curve gives a total weight loss of about 60% at 900 °C, which is slightly less than the corresponding calculated total organic mass percentage i.e. 61.9% (6 CO, 2 Cp and 6 R with R = Ph). The X-ray powder pattern of the calcined clusters **a** and **b** revealed the formation of the Mo_2Pd_3 alloy (JCPDS card n°03-065-6263). This result suggests that some molybdenum phosphide (MoP_2) and red phosphorous could sublime during the decomposition of the clusters [27]. In the case of cluster **a**, decomposition of the triethylphosphine ligands is easier than that of the triphenylphosphine ligands of cluster **b**.

With the aim to study the influence of the pore organization during the formation of the metal nanoparticles, we choose two different silica matrices, a matrix SMO of the SBA-15 family and a commercial disordered xerogel. The organized mesoporous matrix SBA-15 possesses an hexagonal arrangement of cylindrical pores with a narrow pore size distribution centred around ca. 6 nm. The xerogel used is a porous silica matrix whose pores do not present a particular arrangement except for a bimodal pore size distribution centred around 4.0 and 6.3 nm, respectively. The four different samples **1a**, **1b**, **2a** and **2b** are presented below and their physical characteristics are listed in Table 1.

Characterisation of the Impregnated Samples

We studied the thermal behaviour of the impregnated clusters under the same conditions as those used for the clusters alone. The four samples (**1a**, **1b**, **2a** and **2b**)

Table 1 Physical characteristics of the host matrices before and after impregnation followed by a calcination

Sample	Unit cell parameter a (nm) after calcinations[a]	S_{BET}^{b} (m^2/g)	$\varnothing$ pores[c] (nm)	Wall thickness (nm)[d]	V_t (cm^3/g)[e]	V intra grain
SBA-15	12.1	920	6.7	5.4	1.09	1.06
1a	12	62	4.6		0.108	0.058
1b		70	4.2		0.30	0.07
Xerogel 40–63 μm	/	502	4.0 and 6.3	/	0.71	
2b	/	84	4.0 and 6.3	/	0.29	
2a	/	80	4.0 and 6.3	/	0.20	

[a] Determined by XRD

[b] S_{BET} BET surface area

[c] Determined from the desorption branch by the BJH method

[d] Thickness of the walls calculated from the relation: a—pore diameter
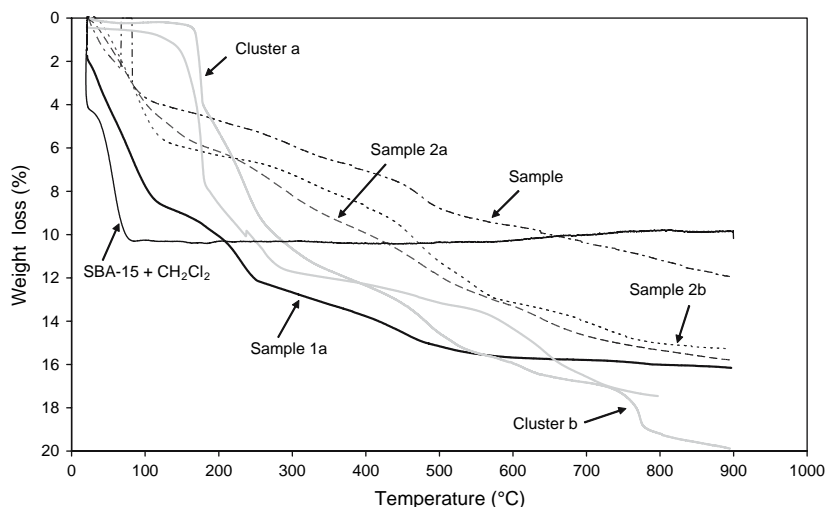
[e] Total porous volume

Fig. 3 Thermogravimetric analysis of samples **1a**, **1b**, **2a** and **2b** after impregnation and of the blank (SBA-15 containing CH_2Cl_2). The grey solid lines are the TG curves of bulk clusters **a** and **b** (the scale has been divided by a factor of 3 to allow a better comparison)

have a similar thermal behaviour. A SBA-15 blank containing CH_2Cl_2 prepared in the same way as the four samples (Fig. 3) but without cluster impregnation showed that all the dichloromethane was totally desorbed above 90 °C. Therefore, weight losses occuring above 90 °C are attributed to the decomposition of the impregnated clusters. Above this temperature, the curve becomes different to those obtained with the bulk clusters **a** or **b** (Fig. 3). The total organic weight losses should be of 9.3, 12.8, 10.8 and 11.0% for samples **1a**, **2a**, **1b** and **2b**, respectively, and the corresponding experimental values are reported in Table 2. These experimental weight losses are less by 1% higher than the expected ones, except for samples **1b** where the difference is slightly lower. Therefore, the thermal behaviour of the impregnated samples follows that of the pure complexes in term of weight losses i.e. during the thermal treatment, and the sublimation of molybdenum phosphides and phosphorous should occur as in the case of the pure clusters.

The samples were also characterized by powder X-ray diffraction. The low angle part of the patterns of sample **1a** and **1b** are characteristic of the hexagonal mesophase

Table 2 Expected and experimental weight losses deduced from the TG curves of Fig. 3

Samples	Theoretical total organic mass percentage (%)	Experimental weight loss (%)[a]	Experimental total weight loss (%)
1a	9.3	9.8	16.1
2a	12.8	12.8	15.8
1b	10.8	8.9	11.9
2b	11.0	11.9	15.3

[a] % taken from the corresponding TG curves between 90 °C and 900 °C and calculated after subtraction of the weight loss occuring before 90 °C which is supposed to be due to solvent loss
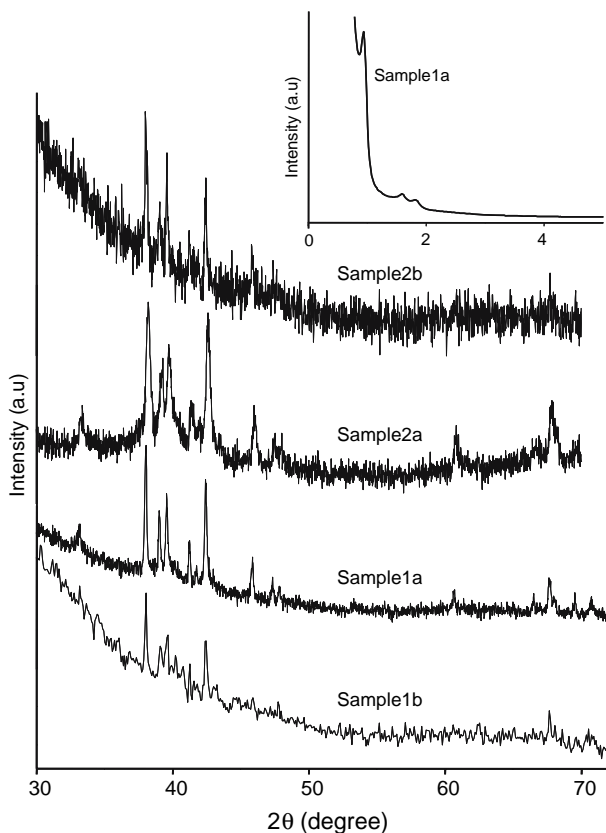
Fig. 4 Powder X-ray diffraction powder patterns of samples **1a**, **1b**, **2a** and **2b** after heat treatment at 900 °C, the insert shows the low angle part of the PXRD patterns of samples **1a**

SBA-15 and demonstrates that the different treatments did not alter the porosity of the matrix (Fig. 4). At higher angles the pattern seems comparable to that of Mo_3P (JCPDS card n°89-2587). The indexation of the pattern makes it possible to obtain the unit cell parameters (Table 3), which are close to those of Mo_3P.

The observation by transmission electronic microscopy of sample **1a** and **1b** shows metallic nanoparticles of small size inside the mesostructure. From the analysis of a traditional TEM image, the repartition seems to be homogeneous, while the particle size distribution plot is centered around 6.5 nm (Fig. 5). This value fits well the pore diameter of the SBA-15 silica matrix (Fig. 6). As far as the pore loading suggested by the N_2 adsorption measurement is concerned (Table 1), clarification will be provided

Table 3 Unit cell parameters of Mo_3P [29] and of sample **1a**

	Mo_3P^a	Sample **1a**
$a = b$ (Å)	9.794	9.786(1)
c (Å)	4.827	4.821(1)
V (Å^3)	463.02	461.7(1)

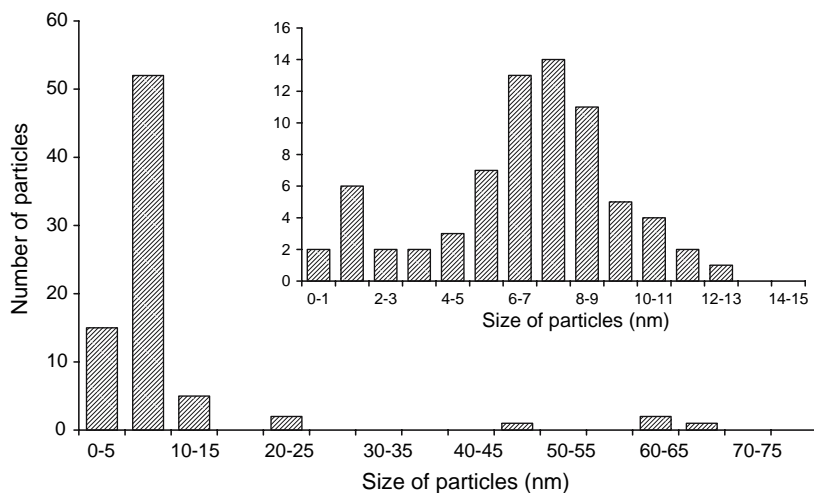[a] The unit cell parameters uncertainties are not indicated in reference [29]

Fig. 5 Histogram of the nanoparticles sizes distribution of sample **1a**
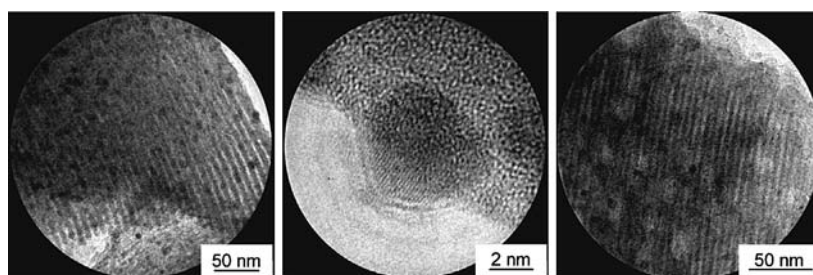

Fig. 6 TEM images of sample **1a** showing the particles insides the pores (left) and a magnification on one nanoparticle (middle), sample **1b** (right)

below by the 3D analysis. For both samples **1a** and **1b**, the free volume decreases by a factor of 90% and 70% after impregnation, respectively, in comparison with the parent SBA-15 matrix. The difference is due to a lower loading in sample **1b** as shown in the PXRD patterns (Fig. 4). With samples **2a** and **2b** however, large nanoparticles are observed (Table 4 and Fig. 7). The N_2 adsorption measurements (Table 1) gave a free volume loss less important by about 65% and this may be explained by the non-organised and tortuous porosity of the xerogel which involves a more significant closing of the apertures at the surface of the xerogel particles during the impregnation and thus leads to a lower loading of clusters.

Table 4 Size of the particles for the different samples

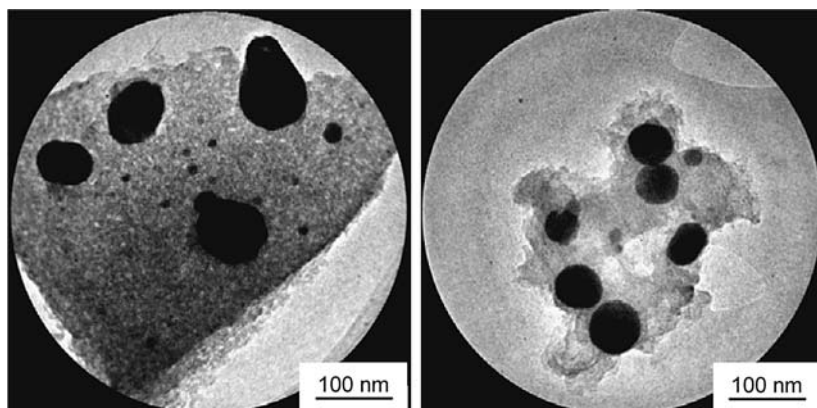| Sample	Particles size
1a	$\varnothing \approx 6.5 \pm 5$ nm
2a	$20 < \varnothing < 120 \pm 15$ nm
1b	$2 < \varnothing < 7 \pm 2$ nm
2b	$80 < \varnothing < 100 \pm 8$ nm

Fig. 7 TEM images of samples **2a** (left) and **2b** (right)

The chemical analyses carried out by the TEM nanoprobe directly on the nanoparticles indicate that they contain Mo, Pd, and P and correspond to the chemical formula Pd_xMo_yP where $1.6 < x < 4$, $0.4 < y < 0.9$. The chemical analyses reported in the Supplementary Material showed some heterogeneities between all the nanoparticles examined in the different samples (SBA-15 (**1a**, **1b**) and xerogel matrices (**2a**, **2b**)). However, whatever the samples, the majority of the nanoparticles responsible of the powder X-ray diffraction patterns plotted on Fig. 4, consist of new ternary compounds isostructural with Mo_3P and with variable chemical compositions where $x + y < 3$. Ternary molybdenum phosphides have been already published in the Mo–Ni–P system [28] and one of them, $Mo_{2.675}Ni_{0.325}P$, is isostructural with Mo_3P [29]. Thus, we simulated a theoretical powder X-ray diffraction pattern on the basis of this model and we have fit it to the experimental pattern of the best crystallized sample **1a**. We used the atomic coordinates of $Mo_{2.675}Ni_{0.325}P$ (space group I4) isostructural with Mo_3P for the calculation. In these structures, there are three distinct crystallographic Mo sites. The atomic numbers and radii of Mo and Pd atoms being 42, 136.3 pm and 46, 137.6 pm, respectively, the scattering powers of both atoms are similar. Consequently, the only variable was the site occupancy factors (s.o.f.) of the Mo atoms. Several models were taken into account concerning the position of the holes but the best solutions indicated that all the three crystallographic Mo sites must be considered. In Table 5 are listed the possible site occupancy factors for the new ternary phase. The corresponding chemical formula, $Pd_{1.7}Mo_{0.4}P$, is close to the mean formula found for sample **1a** (Fig. 8). Unfortunately, a Rietveld refinement

Table 5 Occupancy factors for Mo_3P and $Pd_{1.7}Mo_{0.4}P$

	Mo_3P [24, 25]	$Pd_{1.7}Mo_{0.4}P$
Mo_1	1	0.7
Mo_2	1	0.75
Mo_3	1	0.66
P	1	1

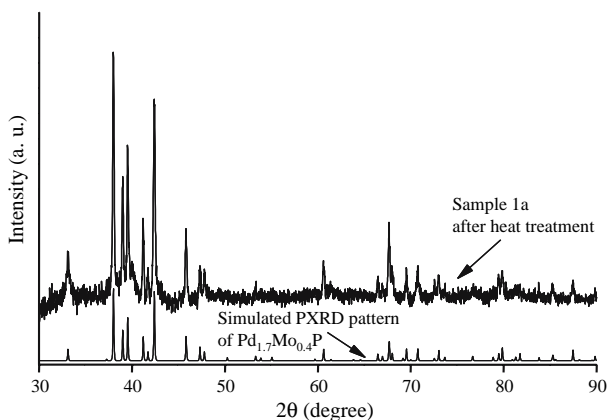**Fig. 8** High angle part of the powder X-ray diffraction powder patterns of sample **1a** and simulated pattern of $Pd_{1.7}Mo_{0.4}P$ from the $Mo_{2.675}Ni_{0.325}P$ atomic coordinates [28]

was not possible in our case owing to the low loading of the phosphide phase inside the samples and consequently, the too low resolution of the PXRD pattern. However, in the present study the new ternary phosphide is necessarily lacunar.

The 3D TEM technique confirmed the presence of the Pd_xMo_yP nanoparticles inside the mesopores. A typical 2D TEM image (one of the projections used to reconstruct the volume of the object) from the tilt series is given in Fig. 9a. Apart from gold fiducial markers, the Pd_xMo_yP nanoparticles are not really visible in such a 2D image. Nevertheless, the analysis of the reconstructed volume confirms the presence of individual metal nanoparticles instead of aggregates (Fig. 9b), because in this case the signal-to-noise ratio is higher than in the initial projections, thanks to the redundancy of information coming from a series of several projections. For visualization, surface renderings were obtained using an intensity-based segmentation procedure from the reconstructed volume in order to select contributions from the silica matrix SBA-15, the Pd_xM_yP and gold nanoparticles. The model as obtained is presented in Fig. 10. According to the results obtained by counting the particles, almost all of the palladium particles observed in the reconstruction (with a diameter higher than the resolution limit of the technique in our experimental conditions, about 2 nm) was located within the channel of the SBA-15 matrix. A qualitative analysis of the particle sizes gave a mean size of about 4 ± 1.5 nm for sample **1a**, close to that determined from the above classical TEM study. The analysis of the geometrical positions of the $Pd_{1.8}Mo_{0.5}P$ nanoparticles shows that their distribution inside the mesopores is relatively homogeneous, with a density of about $17 \pm 5 \times 10^3$ μm^{-3} (sample **1a**).

The IR-FT spectrum of calcined and non-impregnated SBA-15 displays broad absorption bands centered around 3400 cm^{-1} and characteristic of $v(OH)$ vibrations and strong, broad bands between 1,800 cm^{-1} and 400 cm^{-1}. After impregnation of the cluster, additional weak bands are observed at 3,000, 2,060 and 1,970 cm^{-1}, characteristic of $v(CH)$ stretching vibrations (Fig. 11). Their weak intensity is due to the small amount of cluster included in the matrices. The $v(CO)$ vibrations overlap
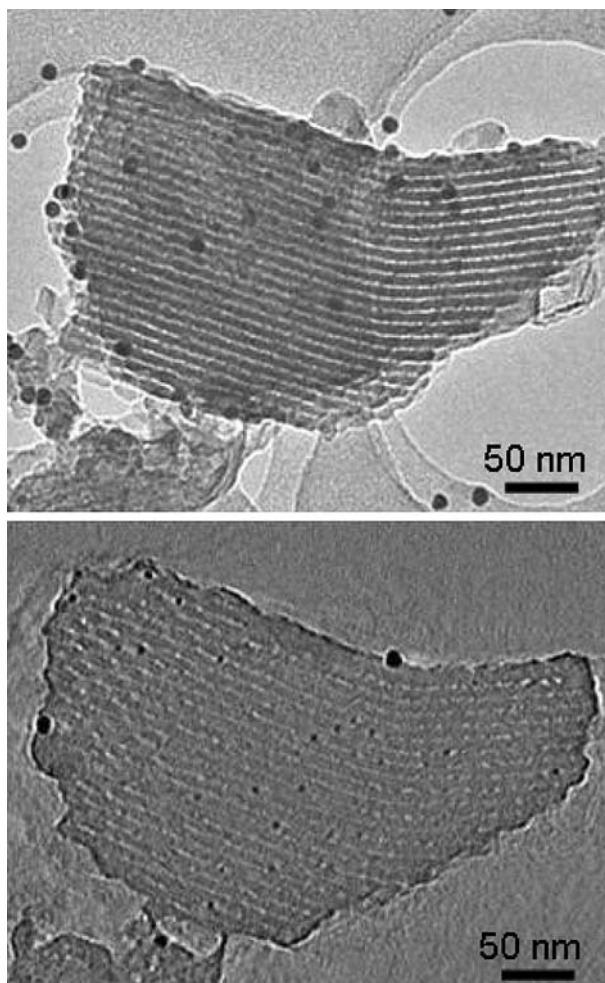
Fig. 9 Typical 2D TEM image (top) (one of the projections of the sample **1a**) from the tilt series used to reconstruct its volume. The bigger and round-shaped particles with 10 nm in diameter are the gold particles deposited on the grid supporting the sample for 3D TEM calibration. A section through the reconstructed volume (bottom) highlighting the presence of the $Pd_{1.8}Mo_{0.5}P$ nanoparticles inside the SBA-15 mesopores

with a strong absorption band at 1,700 cm^{-1}. After thermal treatment under a reducing atmosphere, the v(CH) bands disappear together with the strong v(OH) absorption owing to the thermal decomposition of the cluster and the dehydroxylation of the silica matrix [30], respectively.

Conclusion

In this study, we have described the impregnation of bimetallic clusters onto silica matrices (SBA-15 and xerogel). After a suitable thermal treatment, nanoparticles of
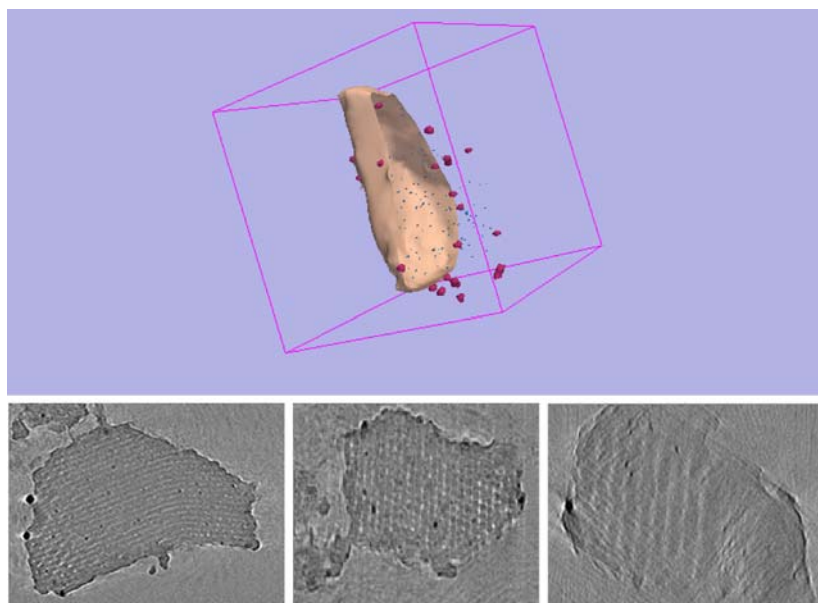
Fig. 10 View of the 3D reconstruction model (top) as well as three orthogonal sections through the reconstruction (bottom) of the whole system showing the homogeneous repartition of the $Pd_{1.8}Mo_{0.5}P$ nanoparticles (in blue) inside the mesopores (in red, gold particles; pink, the outer surface of the SBA-15 particle)
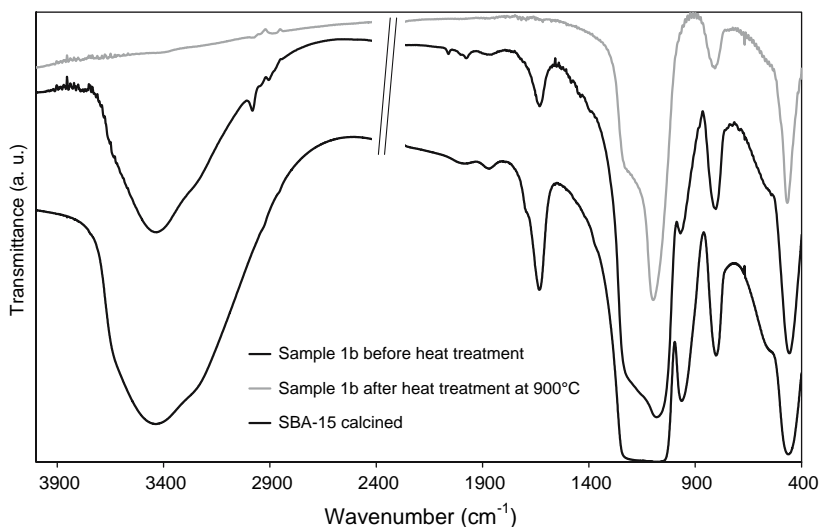

Fig. 11 FTIR spectra of samples **1b** before and after heat treatment compared with pure calcined SBA-15

a new bimetallic phosphide phase were crystallized whatever the phosphine ligand was (PEt_3 or PPh_3). The new ternary compound of formula Pd_xMo_yP is isostructural with Mo_3P but lacunar. The use of an ordered mesoporous silica matrix like the

SBA-15 material is ideal to obtain nanoparticles with a narrow size distribution confined and dispersed in the pores of the mesoporous hosts. However, larger particles were obtained in the case of a non-organised xerogel matrix, which presents a polydisperse pore size distribution. These results open many interesting prospects in solid-state inorganic chemistry and for applications in e.g. heterogeneous catalysis [6]. Furthermore, the formation of bimetallic particles with different compositions could be envisaged starting from the closely related bimetallic clusters $Pd_2M_2Cp_2(CO)_6(PR_3)_2$ with M = Cr and W and R = Me, Et, n-Bu or Ph [19].

References

1. C. T. Kresge, M. E. Leonowicz, W. J. Roth, J. C. Vartuli, and J. S. Beck (1992). *Nature* **359**, 710.
2. (a) P. Braunstein, L. A. Oro, and P. R. Raithby (eds), *Metal Clusters in Chemistry*, (Wiley–VCH, Weinheim, 1999), Vols. 1–3. (b) C. Copéret, M. Chabanas, R. Petroff Saint-Arroman, and J. M. Basset (2003). *Angew. Chem. Int. Ed.* **42**, 156; (c) N. Toshima, and T. Yonezawa (1998). *New J. Chem.*, 1179.
3. D. Zhao, J. Feng, Q. Huo, N. Melosh, G. H. Fredrickson, B. F. Chmelka, and G. D. Stucky (1998). *Science* **279**, 548.
4. D. Zhao, Q. Huo, J. Feng, B. F. Chmelka, and G. D. Stucky (1998). *J. Am. Chem. Soc.* **120**, 6024.
5. P. Braunstein, R. Bender, and J. Kervennal (1982). *Organometallics* **1**, 1236.
6. (a) P. Braunstein, and J. Rosé, *in* R. D. Adams, and F. A. Cotton (eds.) *Catalysis by Di- and Polynuclear Metal Clusters*. (John Wiley, New-York, 1998), pp. 443–508; (b) P. Braunstein, and J. Rosé, *in Metal Clusters in Chemistry* (Wiley–VCH, Weinheim, 1999), Vols. 2, pp. 616–677; (c) P. Braunstein, R. Devenish, P. Gallezot, B. T. Heaton, C. J. Humphreys, J. Kervennal, S. Mulley, and M. Ries (1988). *Angew. Chem., Int. Ed. Engl.* **27**, 927; (1988). *Angew. Chem.* **100**, 972.
7. (a) S. Hermans, T. Khimyak, R. Raja, G. Sankar, J. M. Thomas, and B.F.G. Johnson (2004). *Nanotech. Catal.* **1**, 33; (b) R. D. Adams, and B. Captain (2004). *J. Organomet. Chem.* **689**, 4521; (c) V. Pârvulescu, C. Anastasescu, and B. L. Su (2004). *J. Mol. Catal. A: Chem.* **211**, 143; (d) J. M. Thomas, B.F.G. Johnson, R. Raja, G. Sankar, and P. A. Midgley (2003). *Acc. Chem. Res.* **36**, 20.
8. A. M. Eberhardt, E. V. Benvenutti, C. C. Moro, G. M. Tonetto, and D. E. Damiani (2003). *J. Mol. Catal. A: Chem.* **201**, 247.
9. J. Tetenyi, and V. Galsan (2002). *React. Kinet. Catal. Lett.* **77**, 347.
10. Z. Paal, T. Koltai, K. Matusek, J.-M. Manoli, C. Potvin, M. Muhler, U. Wild, and P. Tetenyi (2001). *Phys. Chem. Chem. Phys.* **3**, 1535.
11. R. Navarro, B. Pawelec, J. L. G. Fierro, and P. T. Vasudevan (1996). *Appl. Catal. A: Gen.* **148**, 23.
12. M. Saïd Zina, and A. Ghorbel (2004). *Solid State Sci.* **6**, 973.
13. B. Pawelec, R. Navarro, J. L. G. Fierro, J. F. Cambra, F. Zugazaga, M. B. Gueemez, and P. L. Arias (1997). *Fuel* **76**, 61.
14. F. Schweyer, P. Braunstein, C. Estournès, J. Guille, H. Kessler, J.-L. Paillaud, and J. Rosé (2000). *Chem. Commun.* 1271.
15. F. Schweyer-Tihay, C. Estournès, P. Braunstein, J. Guille, J.-L. Paillaud, M. Richard-Plouet, and J. Rosé (2006). *Phys. Chem. Chem. Phys.* **8**, 4018.
16. F. Schweyer-Tihay, P. Braunstein, C. Estournès, J. L. Guille, B. Lebeau, J.-L. Paillaud, M. Richard-Plouet, and J. Rosé (2003). *Chem. Mater.* **15**, 57.
17. S. L. Brock, S. C. Perera, and K. L. Stamm (2004). *Chem. Eur. J.* **10**, 3364.
18. M. B. Fernandez, C. M. Piqueras, G. M. Tonetto, G. Crapiste, and D. E. Damiani (2005). *J. Mol. Catal. A: Chem.* **233**, 133.
19. (a) R. Bender, P. Braunstein, J. M. Jud, and Y. Dusausoy (1983). *Inorg. Chem.* **22**, 3394; (b) P. Braunstein, R. Bender, and J. M. Jud (1989). *Inorg. Synth.* **26**, 341; (c) R. Bender, P. Braunstein, J. M. Jud, and Y. Dusausoy (1984). *Inorg. Chem.* **23**, 4489.

20. S. Kawi, O. Alexeev, M. Shelef, and B. C. Gates (1995). *J. Phys. Chem.* **99**, 6926.

21. M. C. Carrión, B. R. Manzano, F. A. Jalón, P. Maireles-Torres, E. Rodríguez-Castellón, and A. Jiménez-López (2006). *J. Mol. Catal. A: Chem.* **252**, 31.

22. STOE WinXPOW, version 1.06, 1999.

23. D. N. Mastronarde (1997). *J. Struct. Biol.* **120**, 343.

24. O. Ersen, J. Werckmann, M. Houlle, M.-J. Ledoux, and C. Pham-Huu (2007). *Nano Lett.* **7**, 1898.

25. S. Brunauer, P. H. Emmett, and E. Teller (1938). *J. Am. Chem. Soc.* **60**, 309.

26. E. P. Barrett, L. G. Joyner, and P. P. Halenda (1951). *J. Am. Chem. Soc.* **73**, 373.

27. W. G. Moffatt, *The handbook of binary phase diagrams*, (Genium publishing corporation, 1976–1987), Vols. 1–5.

28. S. V. Oryshchyn, C. Le Sénéchal, S. Députier, J. Bauer, R. Guérin, and L. G. Akselrud (2001). *J. Solid State Chem.* **160**, 156.

29. B. Sellberg, and S. Rundqvist (1965). *Acta Chem. Scand.* **19**, 760.

30. B. A. Morrow, and A. J. McFarlan (1992). *J. Phys. Chem.* **96**, 1395.